SAPO-35 zeolite crystallized using novel structure-directing agent for catalytic conversion of levulinic acid into ethyl levulinate under non-microwave instant heating

Yik-Ken Ma, Stephen Chia, Jean-Louis Paillaud, T. Jean Daou, Fitri Khoerunnisa, Zeinhom El-Bahy, Tau Chuan Ling, Amal Altalhi, Samy Mahmoud, Eng-Poh Ng

SAPO-35 zeolite crystallized using novel structure-directing agent for catalytic conversion of levulinic acid into ethyl levulinate under non-microwave instant heating

Yik-Ken Ma [a], Stephen Chia [b], Jean-Louis Paillaud [c,d], T. Jean Daou [c,d], Fitri Khoerunnisa [e], Zeinhom M. El-Bahy [f], Tau Chuan Ling [g], Amal A. Altalhi [h], Samy F. Mahmoud [i], Eng-Poh Ng [a,*]

[a] *School of Chemical Sciences, Universiti Sains Malaysia, 11800, USM, Penang, Malaysia*
[b] *Centre for Global Archaeological Research, Universiti Sains Malaysia, 11800, USM, Penang, Malaysia*
[c] *Université de Haute-Alsace, Axe Mat´eriaux `a Porosités Contrôlées, Institut de Science de Matériaux de Mulhouse UMR 7361, ENSCMu, 3b Rue Alfred Werner, 68093,Mulhouse, France*
[d] *Université de Strasbourg, 67000, Strasbourg, France*
[e] *Chemistry Education Department, Universitas Pendidikan Indonesia, Jl. Setiabudhi 258, Bandung, 40514, Indonesia*
[f] *Department of Chemistry, Faculty of Science, Al-Azhar University, Nasr City, 11884, Cairo, Egypt*
[g] *Institute of Biological Sciences, Faculty of Science, University of Malaya, 50603, Kuala Lumpur, Malaysia*
[h] *Department of Chemistry, College of Science, Taif University, P.O.Box 11099, Taif, 21944, Saudi Arabia*
[i] *Department of Biotechnology, College of Science, Taif University, P.O. Box 11099, Taif, 21944, Saudi Arabia*

To cite this article: SAPO-35 zeolite crystallized using novel structure-directing agent for catalytic conversion of levulinic acid into ethyl levulinate under non-microwave instant heating, *Materials Chemistry and Physics* **2022**, 287, 126240. DOI : 10.1016/j.matchemphys.2022.126240 , HAL : hal-03826150.
Received 26 December 2021; Received in revised form 8 April 2022; Accepted 6 May 2022; Available online 11 May 2022

Keywords: SAPO-35, zeolite, 1-propylpyridinium hydroxide, ethyl levulinate, non-microwave instant heating

ABSTRACT: SAPO-35 zeolite (LEV topology) is an 8-membered ring zeolite material that offers high selectivity and activity in separation and catalysis but this microporous material can only be crystallized using hexamethyleneimine, quinuclidine and cyclohexylamine organic templates thus far. Herein, the hydrothermal synthesis and crystallization evolution of SAPO-35 using a novel *N*-heterocyclic organic template, namely 1-propylpyridinium hydroxide ([PPy]OH), are reported. As compared to the previous reported hexamethyleneimine-templated synthesis conditions (24 h, 200 °C), the current system requires merely 21 h to fully crystallize SAPO-35 using [PPy]OH new template. Furthermore, the current system also witnesses a different route for crystallizing SAPO-35 where dissolution of reactants (induction), nucleation, crystal growth and intrazeolite transformation from SAPO-34 to SAPO-35 are observed. The resulting SAPO-35 zeolite of high porosity and acidity is active and selective in the catalytic conversion of levulinic acid into ethyl levulinate–a biofuel additive–under nonmicrowave instant heating, where it shows 96.3% conversion and 100% selectivity towards ethyl levulinate after 20 min at 190 ◦C with high catalyst reusability. Hence, this work offers a promising route to crystallize SAPO-35 that is benign for catalytic biofuel upgrading.

1. INTRODUCTION

Aluminophosphate (AlPO-*n*) is a class of zeolite material with neutral surface charge that is formed by strictly alternating $[AlO4]^-$ and $[PO4]^+$ monomer units [1]. By incorporating silicon (Si) atoms into the AlPO-n framework, it gives rise to the formation of acid sites in silicoaluminophosphates (SAPO-*n*) that are essential for broad industrial applications [2–4]. These zeotypes have been proven as promising candidates as selective water adsorbents [5], and catalysts in the methanol-to-olefins (MTO) reaction [6], hydroisomerization of long-chain paraffin [7,8], dewaxing [9], isomerization [10], hydrodeoxygenation (HDO) of vegetable oils [11], n-alkane cracking [12], and oxidative dehydrogenation of ethane [13].

So far, there have been more than 50 types of SAPO-*n* with unique framework structures discovered and synthesized [14]. Among them, SAPO-35 (LEV topology) is one of the important SAPO-*n* materials. This small-pore zeotype material (3.6 × 4.8 $Å^2$) is made up of levyne cages that are connected through single six rings (S6R) and double six rings (D6R) where its adequate pore size and shape allow selective molecular diffusion and separation for linear hydrocarbons [15]. Nevertheless, the research into the synthesis and application of SAPO-35 is relatively scarce due to its rigid synthesis conditions.

SAPO-35 zeolite was first synthesized at 200 °C for 7 days using quinuclidine as an organic template [16]. Then, SAPO-35 was crystallized with the assistance of cyclohexylamine and hydrofluoric acid in a very narrow range of silicon concentration where SAPO-17 as

a competing phase was observed [17]. Meanwhile, cobalt-aluminophosphate LEV molecular sieve named DAF-4 was also prepared using 2-methylcyclohexylamine organic template heating at 200 °C for 7 days [18].

Recently, the use of more reactive template, namely hexamethyleneimine has successfully reduced the crystallization time of SAPO-35 from 7 days to 98 h [19] and 24 h [15,20,21]. It is worth to note that the use of aliphatic aminic structure-directing agents so far still requires long heating times for crystallizing SAPO-35. Hence, seeking more reactive structure-directing agents for rapid crystallizing SAPO-35 with superior surface properties (e.g. high porosity, high framework Si content, high surface acidity) is worth to be further studied.

Herein, the use of *N*-heterocyclic pyridinium compound as a novel organic template for crystallizing SAPO-35 is reported. It is worth to mention here that unlike conventional synthesis route, the current system undergoes different crystallization route where SAPO-34 is first formed from the amorphous solid before intrazeolite transformation occurs forming SAPO-35. The catalytic behavior of SAPO-35 with high porosity and surface acidity is then investigated in esterification of levulinic acid into ethyl levulinate (a biofuel additive [22]) under non-microwave instant heating, where this mode of heating uses SiC heat superconductor to provide rapid and uniform heating, mimicking the microwave heating [23].

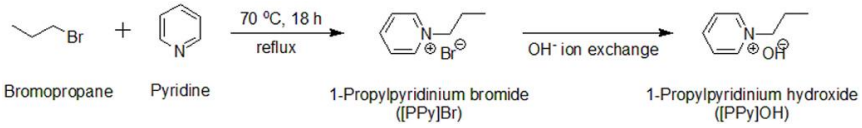

Scheme 1. Synthesis route of 1-propylpyridinium hydroxide ([PPy]OH).

2. Experimental section

2.1 Synthesis of 1-propylpyridinium hydroxide ([PPy]OH) SDA solution

1-Propylpyridinium hydroxide ([PPy]OH) was prepared as follows as in Scheme 1. Typically, pyridine (58.708 g, 99.5%, Merck) and 1-bromopropane (136.925 g, 99%, Merck) in a molar ratio of 1:1.5 were first mixed in a 250-mL round bottom flask. Then, the mixture was heated in an oil bath at 70 °C for 18 h before being rotary evaporated at 90 °C to remove the non-reacted 1-bromopropane. The resulting 1-propylpyridinium bromide ([PPy]Br) ionic liquid was washed with 20 mL of acetone (Qrec) for five times before it was dried in an oven at 100 °C overnight. Yield 90.2%. ^{1}H NMR (400 MHz, D_2O): δ = 1.03 (3H, t, *J* = 7.4 Hz, pyridine N–CH_2–CH_2–CH_3), 2.13 (2H, m, *J* = 7.3, pyridine N–CH_2–CH_2–CH_3), 4.71 (2H, t, *J* = 7.25 Hz, pyridine N–CH_2), 8.19 (2H, t, *J* = 6.5 Hz, pyridine N–CH═CH), 8.66 (1H, t, *J* = 7.75 Hz, pyridine N–CH═CH–CH), 8.98 (2H, d, J = 5.9 Hz, pyridine N═CH). FTIR (KBr disk) cm^{-1}: 1170 (C–N), 1489 (C═N), 1504 and 1633 (aromatic C═C), 2879 (C^3_{sp}-H), 3056 (C^2_{sp}-H), 3400 cm^{-1} (broad, O–H). Anal. Cacld. For $C_8H_{12}NBr$: C, 47.55%; H, 5.94%; N, 6.93%; found: C, 46.81%; H, 5.85%; N, 6.83%.

The 1-propylpyridinium hydroxide ([PPy]OH) template solution was prepared *via* ion-exchange of [PPy]Br using the Amberlyst® IRN-78 ion-exchange resin in hydroxide (OH^-) form (Acros Organic). The Amberlyst IRN-78 ion exchange resin is an insoluble polymeric resin in yellowish microbeads form (diameter ca. 0.90 mm) that possess high porosity that provides large surface area enabling efficient ion exchange [24]. Typically, 50.000 g of resin and 50.000 g of [PPy]Br were added into 50.000 g of distilled water before the ion-exchange process was initiated (16 h, 200 rpm). After the treatment, the resin was separated from the template solution using vacuum filtration. The %OH^- conversion of the template solution was determined by titrating 1 mL of filtrate with 0.1 M of HCl. The ion exchange and titration process were repeated for several cycles until the %OH^- reached at least 85%. Finally, the template solution was concentrated to 32.86% in water under oven evaporation (60 °C) before it was readily used as an organic template for the crystallization evolution study of SAPO-35.

2.2 Formation study of SAPO-35

SAPO-35 microporous solid was crystallized in the presence of [PPy] OH as the structure-directing agent. Typically, aluminum isopropoxide (0.625 g, 98%, Acros Organics) was dissolved in the [PPy]OH template solution (4.500 g, 89.7% OH^- exchanged) under vigorous stirring (600 rpm, 30 min). Then, distilled water (0.835 g) and orthophosphoric acid (0.806 g, 85%, Merck) were mixed and slowly added dropwise into the solution to avoid the formation of large and dense particles; the addition process took about 30 min. Next, tetraethyl orthosilicate (0.277 g, 98%, Sigma-Aldrich) was added and the resulting mixture was further stirred for 5 min to produce a precursor hydrogel with a molar composition of $1Al_2O_3$:$2.33P_2O_5$:$3.34[PPy]_2O$:$0.87SiO_2$$148H_2O$. The precursor was then transferred into a 15-mL Teflon-lined stainless-steel autoclave, capped and subjected to hydrothermal treatment at 200 °C for different time intervals (0-21 h). The crystallization was interrupted, and the autoclave was cooled down to room temperature under running water. The precipitated solid was recovered using high-speed centrifugation (10000 rpm, 8 min) followed by washing with distilled water until pH 7 before the solid product was dried (80 °C, 14 h) and calcined (600 °C, 6 h, 1 °C/min) under air flow.

2.3 Characterization

The crystallinity and phase purity of the samples were confirmed by using a Bruker D8 AVANCE diffractometer (Cu Kα radiation, 2θ = 4–40°, λ = 0.15418 nm, 40 kV). The crystal size and morphology of the solid products were studied using a Leo Supra 50VP field emission scanning electron microscope (FESEM) operated at 30 kV. Prior to measurement, the sample was sputtered with gold to prevent charging. The functional groups of the samples were investigated using a PerkinElmer's System 2000 IR spectrometer. The spectra were recorded in the wavenumber of 1600–400 cm^{-1} using the KBr method (KBr:sample ratio = 50:1). The elemental analysis of sample was performed using the ICP-OES spectroscopy (Vista MPX, Varian Inc.). Prior to analysis, the sample (5 mg) was first stirred and dissolved in concentrated HF solution (47%, 5 mL) for 14 h before the resulting solution was top-up to 250 mL. Boric acid (1.000 g, Merck) was also added for minimizing the fluoride interference during the ICP-OES analysis. The porous properties of SAPO-35 was studied with a Micrometrics ASAP 2010 nitrogen adsorption analyzer. Prior to analysis, the powder sample was first outgassed at 250 °C for 4 h under vacuum before the adsorption analysis was initiated at −196 °C. The organic and inorganic moieties in the as-synthesized SAPO-35 sample were investigated using a PerkinElmer's TGA 4000 thermogravimeter (heating rate 20 °C/min) under air flow conditions. The amount and strength of surface acid of SAPO-35 were determined by the temperature program desorption analysis probed with NH_3 (NH_3-TPD). Before analysis, the sample (ca. 0.008 g) was first outgassed in a BELCAT-B analyzer (400 °C, 8 h, He flow). The system was then saturated with NH_3 gas to allow adsorption before the desorption analysis acquisition was initiated from 50 to 700 °C at a heating rate of 10 °C/min.

2.4 Catalytic study

The catalytic biomass upgrading study was carried out via esterification of levulinic acid into ethyl levulinate using a novel nonmicrowave instant heating technique. Initially, 0.025 g of activated SAPO-35 zeolite (200 °C, 3 h), levulinic acid (0.040 g, 98%, Acros Organics) and ethanol (0.170 g, 99.7%, Acros Organics) in the molar ratios of 1:11 were added into a glass vial. The levulinic acid:ethanol molar ratio of 1:11 was selected because it gave the highest reaction conversion based on our catalytic reaction study and similar observation was also observed by Halder et al. [25,26] where high alcohol content is beneficial for high esterification reaction conversion. The vial was sealed and instantly heated to the desired temperature (150–190 °C) for a specific time (0–60 min) under very fast stirring rate (800 rpm) using an Anton Paar's Monowave 50 non-microwave instant heating reactor; the system required less than 2 min to reach to the desired temperature. After the reaction, the solution was separated and injected into a GC-FID chromatograph (Agilent/HP6890 GC) and GC-MS (Agilent 7000 Series Triple Quad) for product identification and quantitative analyses, respectively; toluene was used as the internal standard. The GC data acquisition was performed using the ChemStation® software while the reaction conversion and selectivity are calculated using Equations (1) and (2) respectively:

$$Conversion\ of\ levulinic\ acid(\%) = \left[\frac{\left(\frac{A_{Levulinic\ acid}}{A_{Toluene}}\right)_{t_0} - \left(\frac{A_{Levulinic\ acid}}{A_{Toluene}}\right)_{t_i}}{\left(\frac{A_{Levulinic\ acid}}{A_{Toluene}}\right)_{t_0}}\right] \times 100\% \qquad \text{(Equation 1)}$$

$$Selectivity\ (\%) = \left[\frac{A_{Ethyl\ levulinate}}{A_{Total}}\right] \times 100\% \qquad \text{(Equation 2)}$$

where $A_{Levulinic\ acid}$ was the peak area of the limiting agent (levulinic acid), $A_{Toluene}$ was the peak area of the internal standard (toluene), t_0 and t_i were the reaction times at 0 h and i h respectively, $A_{ethyl\ levulinate}$ was the peak area of the product (ethyl levulinate), and A_{total} was the total peak area of the products obtained (Figs. S1 and S2).

3. Results and discussion

3.1 Time-dependent crystallization study of SAPO-35

In the first 10 h of hydrothermal heating, no solid product was recovered upon centrifugation indicating that the reactants have undergone dissolution and the resulting precursor is in the induction stage. At this stage, the Si, Al and P reactants hydrolyze forming soluble monomers and oligomers [27]. At 16 h, the precursor solution turned cloudy and some solid was successfully collected indicating polymerization of inorganic species forming denser solid is taking place. Concurrently, the matter exchange between solid and liquid parts occurs, inducing nucleation process [28]. Nevertheless, the solid is amorphous based on the detection of merely an XRD hump at 2θ = 17°–30° (Fig. 1a). According to FESEM microscopy analysis, this amorphous solid is composed of sub-micron sized particles (ca. 93 nm) having non-specific shape (Fig. 2a and b).

With crystallization time further extended for additional 2 h–18 h, the morphology of the solid drastically changed and fast crystallization of

pure SAPO-34 (CHA topology) was observed by the XRD and FESEM analyses (Figs. 1b and 2c,d). This CHA solid is consisted of cubic-like secondary particles (ca. 1.7 µm) formed by smaller primary crystals with size ranging from 0.2 to 1.1 µm. Further heating the precursor solution to 20 h facilitates the intrazeolite transformation of SAPO-34 to SAPO-35 where the XRD peaks assigned to SAPO-35 emerge at the expense of the SAPO-34 XRD peaks (Fig. 1c). Thus, this suggested that the SAPO-34 crystals progressively dissolved in the mother liquor where its double-6-ring (D6R) secondary building units that are contained in the solution are served as a seed (or nuclei) for the growth of SAPO-35, viz. a more metastable crystalline phase [29,30]. This phenomenon is also observed by the FESEM microscopy where the images of cubic-like (SAPO-34) and rhombohedra (SAPO-35) intergrown crystals are captured (Fig. 2e and f).

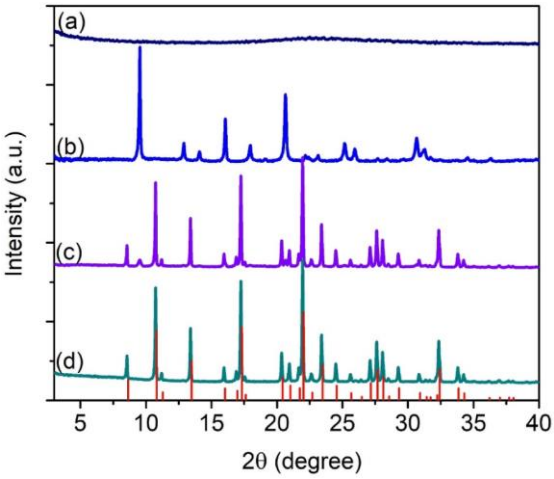

Fig. 1. XRD patterns of samples after (a) 16 h, (b) 18 h, (c) 20 h, and (d) 21 h. The theoretical LEV simulated XRD pattern is shown in red lines. (For interpretation of the references to colour in this figure legend, the reader is referred to the Web version of this article.)

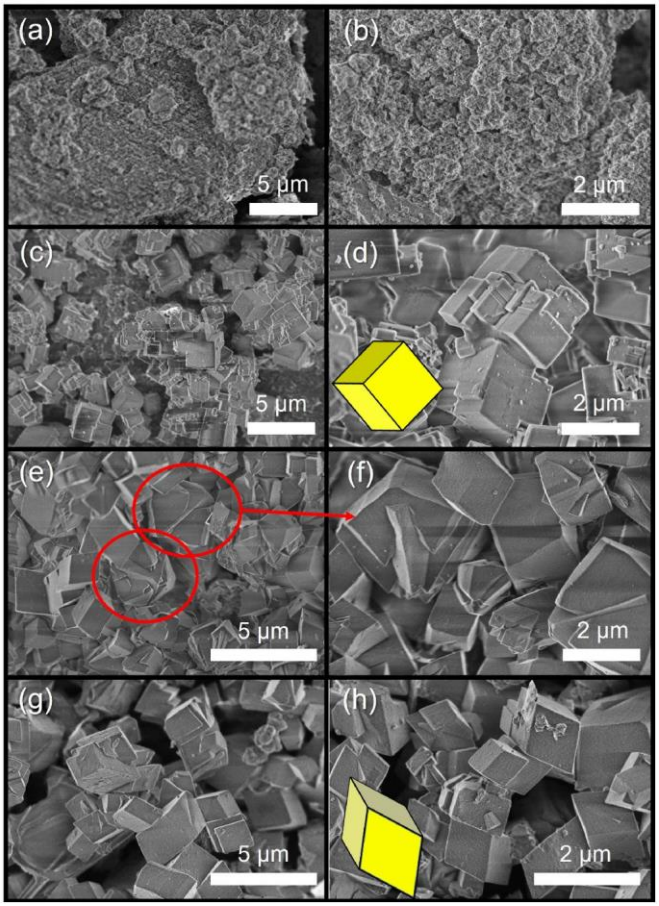

Fig. 2. FESEM images of samples after (a,b) 16 h, (c,d) 18 h, (e,f) 20 h and (g,h) 21 h.

The intrazeolite transformation occurs rapidly where the SAPO-34 crystalline phase completely disappears and transforms into SAPO-35 after 21 h of hydrothermal treatment (Fig. 1d). The XRD pattern of assynthesized SAPO-35 is indexed and compared with the theoretical generated XRD pattern (in red lines). It shows the XRD profile of SAPO-35 is well indexed to the standard diffraction pattern of trigonal LEV crystalline phase suggesting the sample is of very high purity [31]. The FESEM study also agrees with the XRD observation whereby rhombohedra crystals (ca. 1.3 µm) are formed, and the morphology of SAPO-35 synthesized in this work is identical to that reported in literature (Fig. 2g and h) [20,21]. One should note that the proposed method for synthesizing SAPO-35 is reproducible using different batch of [PPy]OH template solution (92.1% OH^- exchanged). The crystallization time was also extended to 28 h. However, co-crystallization of SAPO-35 with SAPO-36 was observed explaining the metastability nature of SAPO-35. The HRTEM images of pure SAPO-35 are shown in Fig. 3. As seen, the SAPO-35 crystals possess rhombohedra shape and the crystallite size is ca. 1.3 µm which agrees with the FESEM analysis (Fig. 2h). Furthermore, a HRTEM image with a very high magnification shows that the interface of SAPO-35 solid is smooth with very sharp edge indicating the SAPO-35 crystals are well formed in the presence of [PPy]OH new templating system [32].

The formation of SAPO-35 was also followed by using IR spectroscopy (1600–400 cm^{-1}) where this technique can easily observe the change in the vibrations of framework and functional groups during the entire crystallization process [33]. The IR spectrum of crystallization time less than 16 h was not recorded since no product was successfully collected. The IR spectrum of sample after 16 h of heating is shown in Fig. 4a where four amorphous characteristic broad absorption bands are detected: 1139 and 726 cm^{-1} are due to asymmetric and symmetric O–P–O stretching, respectively; 566 cm^{-1} is ascribed to bending of P–O in PO4; 484 cm^{-1} corresponds to Al–O bending mode [34,35]. In addition, a very weak IR band due to double-6-ring (D6R) secondary building unit (SBU) also start to be observed at 628 cm^{-1} where this sub-unit is the basic and key component for the construction of AEI, CHA, EMT, FAU KFI, LEV and OFF-type zeolite frameworks [30,35]. Thus, this indicates that the zeolite nucleation has occurred in the hydrogel precursor.

The IR spectrum pattern changes drastically when fast crystallization occurs after 18 h (Fig. 4b). As shown, the IR bands are becoming more resolved, and the IR pattern of this sample is identical to that of SAPO-34 [36]. The IR bands at 1227, 1110 and 1039 cm^{-1} are due to P–O–Al stretching, asymmetric O–P–O stretching and P–O stretching modes, respectively [35]. In addition, the signal at 641 cm^{-1} is assigned to D6R secondary building unit, whereas the bends of PO_4, AlO_4, SiO_4 and T-O (T = Si, Al or P) are shown at 570, 531, 481 and 442 cm^{-1}, respectively [35,37]. When the crystallization is further extended to 20 and 21 h, intrazeolite transformation from CHA (SAPO-34) to LEV (SAPO-35) framework structure occurs where the IR bands of SAPO-34 in the low wavenumber region (760–490 cm^{-1}) completely disappear and change to the IR pattern of SAPO-35 (Fig. 4c and d): 752 cm^{-1} arising from symmetric O–P–O stretching; 688 cm^{-1} due to 4-membered ring; 643 cm^{-1} ascribed to D6R polyhedral unit and 559 cm^{-1} assigned to bending of T-O of TO_4 unit [37]. The stretching vibration of aromatic carbon (C═C) and bending of C–H of pyridinium template are observed at 1492 cm^{-1} and 1456 cm^{-1} respectively [38].

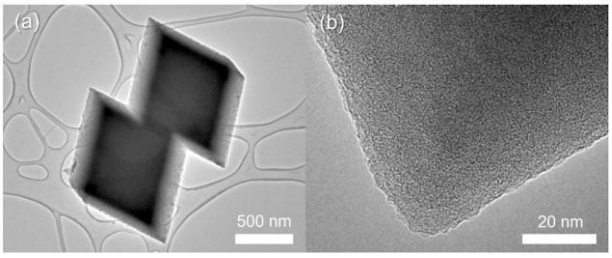

Fig. 3. HRTEM images of as-synthesized SAPO-35 at (a) low and (b) high magnifications.

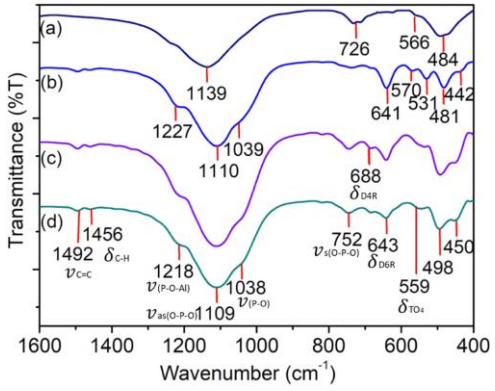

Fig. 4. IR spectra of samples after (a) 16 h, (b) 18 h, (c) 20 h and (d) 21 h.

The role of $[PPy]^+$ as an organic template for directing the formation of SAPO-35 is confirmed by the thermogravimetry analysis. In order to prove this, the TG/DTG profiles of pure [PPy]Br and as-synthesized SAPO-35 were recorded and compared. In general, the free organic template shows a weight loss (3.8%) at <180 °C due to absorbed water, and another two steps of weight loss from 180 to 500 °C are attributed to the decomposition of [PPy]+ organic template (Fig. 5a) [39]. Upon combustion of as-synthesized SAPO-35 at constant heating rate (20 °C/min), the TG/DTG data confirms the presence of $[PPy]^+$ organic template in the micropores of SAPO-35 crystalline solid where a significant delay in the thermal decomposition of $[PPy]^+$ molecule (215–795 °C) can be explained by the strong confinement and chemical interaction between $[PPy]^+$ molecules and LEV framework (Fig. 5b) [40]. From the TG/DTG analysis, it is shown that 20.6% of $[PPy]^+$ is occluded into the LEV micropores, indicating one $[PPy]^+$ molecule is enfolded by 7.7 TO_4 tetrahedral units (T = Si, Al or P) which is fully in line with the theoretical predictions, *viz.* LEV framework rings that are made up of 8 TO_4 tetrahedral oxyanions [31].

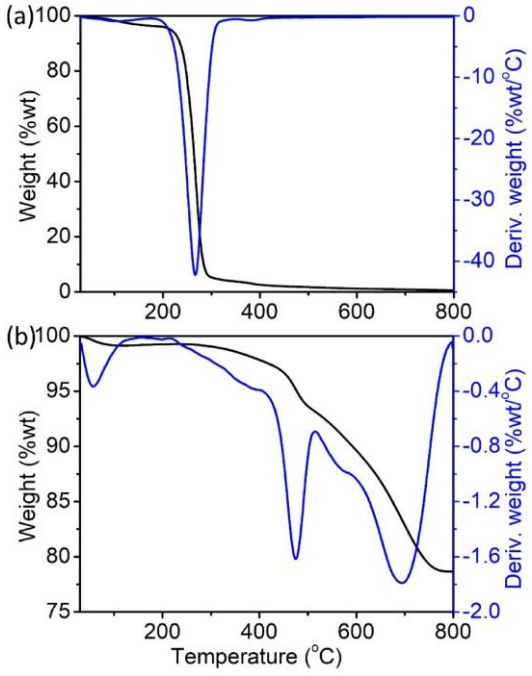

Fig. 5. TGA/DTG of (a) pure [PPy]Br template, and (b) as-synthesized SAPO-35.

3.2 Characterization of SAPO-35 zeolite catalyst

The as-synthesized SAPO-35 (sample crystallized at 21 h) was calcined at 550 °C prior being used in catalytic reaction study. This is to ensure that its porosity is free from occluded organic moiety for enabling molecular diffusion and accessibility. In this respect, the porous properties of SAPO-35 were first studied using the N_2 adsorption-desorption technique at −196 °C. Fig. 6 shows the N_2 adsorption-desorption isotherm and pore size distribution derived from non-local density functional theory (NLDFT) model. The sample exhibited type I adsorption isotherm with high and sharp knee at very low P/P_o (Fig. 6a) confirming the presence of merely microporosity in the SAPO-35 solid (Fig. 6b) [41]. The SAPO-35 has an average pore size of 2.76 nm and high porosity (surface area = 526 m^2/g, total pore volume = 0.26 cm^3/g) where the large levyne cage and textural porosity of SAPO-35 contributes to its high surface area, large average pore size and high pore volume. Such features are appreciated in the catalytic application that require molecular accessibility [42].

Besides high porosity, the Si content in SAPO-35 is important as it serves as the acid sites for a catalytic reaction [43]. Hence, the elemental analysis of SAPO-35 was carried out using the ICP-OES spectroscopy technique (Table 1). The data shows that the synthesized SAPO-35 has a chemical composition of $Si_{0.207}Al_{0.556}P_{0.237}O_2$. The Si/P and P/Al ratios of synthesized SAPO-35 are 0.87 and 0.43, respectively, with a Si/(Si + Al + P) ratio of 0.207 is recorded. Thus, it indicates that SAPO-35 has considerably high content of Si element as compared to the SAPO-35 previously synthesized using hexamethyleneimine, quinuclidine and cyclohexylamine [17,20].

Surface acidity is a crucial factor controlling the intrinsic catalytic reactivity of a solid. Thus, the acidity of SAPO-35 was examined by NH_3-TPD analysis whereby the peak area of the profile is associated with the number of acid sites and the peak position is related to the acid strength [44]. As displayed in Fig. 7, the deconvoluted NH_3-TPD profile reveals the presence of acidity with three different amounts and strengths in the [PPy]OH-synthesized SAPO-35, namely weak (0.25 mmol/g), mild (0.29 mmol/g) and strong (0.57 mmol/g) acid sites. The total acidity of SAPO-35 is calculated to be 1.10 mmol/g and the value is higher than that synthesized using conventional hexamethyleneimine template (0.89 mmol/g) [21].

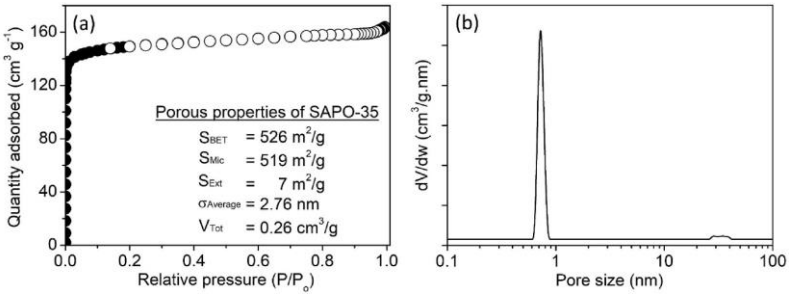

Fig. 6. (a) Nitrogen adsorption-desorption isotherm and (b) pore size distribution of SAPO-35.

Table 1
Chemical composition and acidity of SAPO-35.

Sample	Product composition	Si/P ratio	P/Al ratio	Si content	NH_3-TPD acidity (mmol/g)			
					Weak	Mild	Strong	Total
SAPO-35	$Si_{0.207}Al_{0.556}P_{0.237}O_{2.000}$	0.87	0.43	0.207	0.25	0.29	0.57	1.10

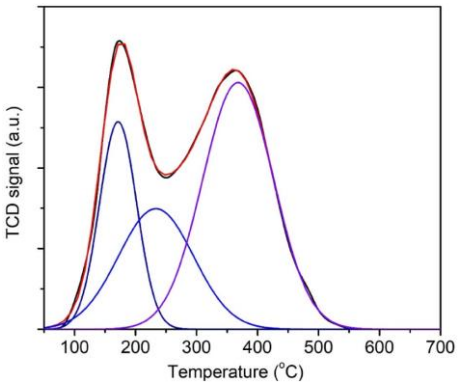

Fig. 7. NH_3-TPD profile of SAPO-35 crystallized using [PPy]OH at 200 °C for 21 h.

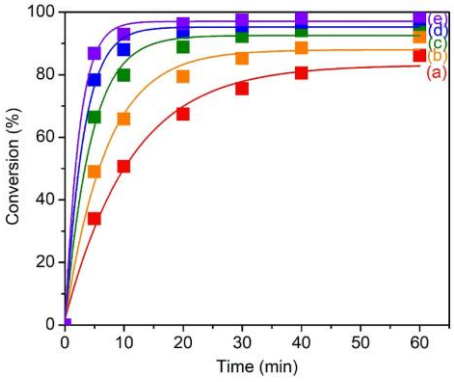

Fig. 8. Esterification of levulinic acid with ethanol catalyzed with SAPO-35 at (a) 150 °C, (b) 160 °C, (c) 170 ◦C, (d) 180 °C and (e) 190 °C under nonmicrowave instant heating. Reaction conditions: Mass of SAPO-35 catalyst = 0.025 g, levulinic acid = 0.33 mmol, ethanol = 3.67 mmol.

3.3 Catalytic reaction study

Esterification of levulinic acid with ethanol under non-microwave instant heating conditions was chosen as a model reaction to evaluate the catalytic behavior of SAPO-35. The reaction was carried out at 150–190 °C from 0 to 60 min and the results are shown in Fig. 8. Without catalyst, the reaction is inactive where 8.5% of levulinic acid is converted into ethyl levulinate at 150 °C after 60 min. Notably, the conversion increases significantly when SAPO-35 catalyst is introduced. At 150 °C, the conversion is tremendously improved to 86.1% with the selectivity to ethyl levulinate remains 100% after 60 min of heating (Fig. 8a). The reaction temperature is further increased to 160 ◦C, 170 °C, 180 ◦C and 190 °C in order to study the effect of reaction temperature where the reaction time is also varied. The reaction temperature was only studied until 190 °C because the reaction pressure will exceed 20 bar beyond 190 °C which will burst the reactor's pressure safety valve. As observed, the catalytic activity of SAPO-35 is enhanced with time and temperature where 79.4%, 88.8%, 93.5% and 96.3% of conversion are achieved after 20 min of reaction at 160 °C, 170 °C, 180 °C and 190 °C, respectively (Fig. 8b–e) [45]. The catalytic reaction enhancement at high temperature is associated with several factors. First, the accessible Brønsted acid sites of SAPO-35 that take part in the esterification reaction where the active sites offer new reaction pathways by enhancing the electrophilicity of carbonyl carbon of levulinic acid via protonation. Second, the SAPO-35 molecular sieve provides an intriguing confinement environment (inner cage size: 6.3 × 7.3 $Å^2$) to the incoming reactants (ethanol: 2.03 × 2.57 × 1.82 $Å^3$, levulinic acid: 2.49 × 1.78 × 5.98 $Å^3$) for the formation of stable transition intermediates, and product molecules (ethyl levulinate: 3.31 × 7.60 × 1.78 $Å^3$) [46,47], whereby structure "breathing" effect and molecular structure distortion allow diffusion for these organic molecules (via head-on orientation) even though their molecular dimensions are close to the pore diameter of SAPO-35 (3.6 × 4.8 $Å^2$) [48,49]. Both effects become more significant especially the reaction is conducted at high temperature. Third, an increase in the reaction conversion is also associated with the chemical kinetics effect since the rate constant increases exponentially with temperature as described by Arrhenius equation [50]. Meanwhile, the external surface is also important in the reaction but not as important as the micropores because the synthesized SAPO-35 has the micropore surface area (519 m^2/g) larger than its external surface area (7 m^2/g). From the catalytic study, the optimum reaction conditions are hence at 190 ◦C for 20 min of heating.

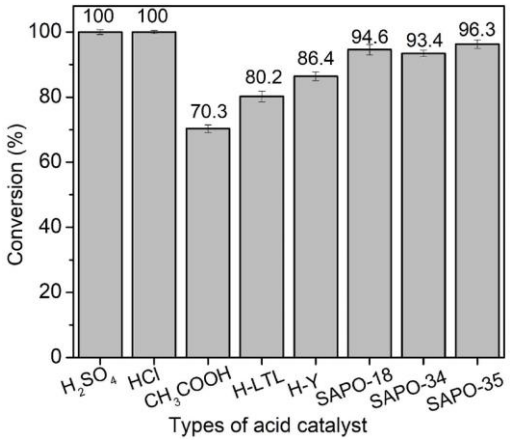

Fig. 9. Comparative catalytic study using different homogeneous and heterogeneous acid catalysts. Reaction conditions: temperature = 190 ◦C, time = 20min, levulinic acid = 0.33 mmol, ethanol = 3.67 mmol, catalyst = 7.70 µmol equivalent to 0.025 g of SAPO-35, 0.001 g of H_2SO_4, 0.001 g of HCl, 0.0005 g of CH_3COOH, 0.0201 g of H-LTL, 0.088 g of H–Y, 0.020 g of SAPO-18 and 0.017 g of SAPO-34, number of experiments = 2.

The catalytic activity of SAPO-35 is also compared with other homogeneous (HCl, H_2SO_4, acetic acid glacial) and heterogenous (SAPO-18, SAPO-34, H-LTL, H–Y) zeolite catalysts where similar molarity of catalyst is used to catalyze this reaction at 190 °C for 20 min. Note: The average crystal sizes of SAPO-18, SAPO-34, H-LTL (Si/Al = 3.2) and H–Y (Si/Al = 2.5) are ca. 3.21 × 0.10 μm^2, 1.76 × 1.85 μm^2, 4.16 × 2.07 μm^2 and 1.17 × 1.31 μm^2, respectively. As seen, concentrated H_2SO_4 and HCl successfully convert all levulinic acid into ethyl levulinate whereas acetic acid only gives 70.3% conversion (Fig. 9). These three catalysts, however, are corrosive, harmful to the environment and not reusable. For SAPO-35, it achieves nearly complete conversion (96.3%) as compared to the corrosive H_2SO_4 and HCl. SAPO-35 also performs slightly better than other 8-membered ring zeolites—SAPO-34 (93.4%) and SAPO-18 (94.6%)—and 12-membered ring aluminosilicate zeolites (H-LTL: 80.2%, H–Y: 86.4%) thanks to its proper pore size that perfectly matches the size of reactants and large amount of surface acidity with medium-to-strong acid strength.

3.4 Proposed mechanism

The proposed reaction mechanism of SAPO-35 zeolite catalyst in esterification of levulinic acid with ethanol is shown in Fig. 10. Initially, the levulinic acid (2.49 × 1.78 × 5.98 $Å^3$) enters the micropores of SAPO-35 (3.6 × 4.8 $Å^2$) via head-on orientation. At high temperature, the micropore opening becomes larger due to "breathing" effect, hence facilitating efficient molecular entrance [48]. The levulinic acid then diffuses and adsorbs on the Brønsted acid site located in the micropore channels and/or at the external surface via electrostatic attraction force (Step 1). Then, the levulinic acid is activated by the Brønsted acid site to form a stabilized carbocation intermediate through delocalization of the positive charge on carbonyl carbon (Step 2) [47]. Meanwhile, the diffusion and adsorption of ethanol on the SAPO-35 surface also takes place via dipole interactions between O–H group of ethanol and the framework oxygen (Step 3), thus bringing it closer to carbocation and facilitates nucleophilic carbocation substitution by ethanol (Steps 4 and 5), yielding ethyl levulinate and water as the products (Step 6) [51]. After the reaction, the products molecules are released from the active sites and diffuse out from the zeolite pores. The active sites are available again to adsorb and react with subsequent incoming reactant molecules (Step 1).

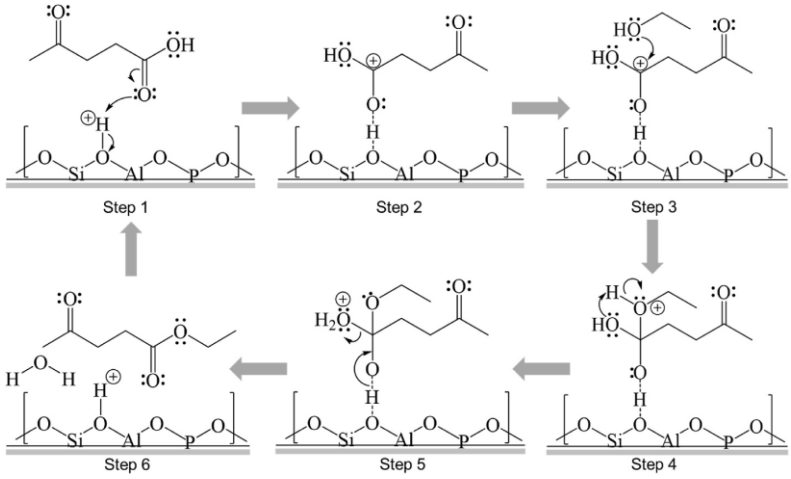

Fig. 10. Possible mechanism of esterification reaction of levulinic acid with ethanol in the presence of SAPO-35 solid acid catalyst.

3.5 Catalyst reusability study

The catalyst recyclability of SAPO-35 was also studied at 190 °C for 20 min in order to determine its stability after ten subsequent reaction cycles. Prior to the study, the used catalyst after the first cycle of reaction was washed with diethyl ether (15 mL × 3 times), air dried and reactivated (350 °C, 4 h) for subsequent uses. The results showed that the SAPO-35 catalyst after the tenth run of reaction recorded 89.2% of conversion where a decrease in the conversion could be due to slight coking after multiple cycles of reaction and slight catalyst loss during recovering process after the completion of catalytic reaction (Fig. 11) [52]. Furthermore, the leaching test was also performed where the reactant mixture containing fresh SAPO-35 catalyst was first stirred at room temperature for 24 h. The solid catalyst was then separated from the liquid and the reactant mixture was reacted under similar reaction conditions (190 °C, 20 min). The GC analysis shows that the reaction only accounted for 11% of conversion. It hence indicates that negligible amount of Si species was detached out from the SAPO-35 framework. The stability of SAPO-35 framework structure after 10 cycles of reaction is further investigated using XRD technique. In general, the XRD peaks intensity slightly decreased but no amorphous hump is observed indicating that the SAPO-35 framework structure is stable after multiple cycles of reaction (Fig. S3). Thus, being not corrosive, reusable, easily handled and stored, this catalyst is considered green and environmentally friendly. In addition, the results indicate that the SAPO-35 molecular sieve serves not only as a good catalyst for producing ethyl levulinate biofuel additive but also offers as a promising material for other advanced applications (e.g. membrane separation, sensor). Comprehensive work on SAPO-35 zeolite in this aspect is in progress.

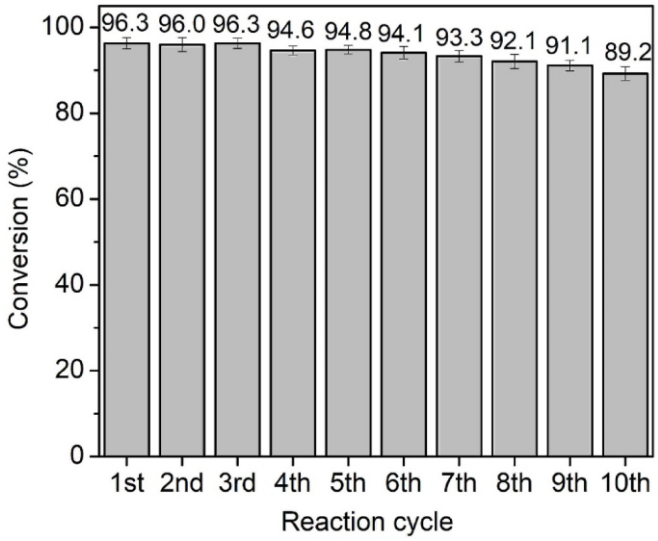

Fig. 11. Catalyst reusability study of SAPO-35 in esterification of levulinic acid with ethanol. Reaction conditions: temperature = 190 °C, time = 20 min, levulinic acid = 0.33 mmol, ethanol = 3.67 mmol, number of experiments = 2. The amounts of levulinic acid and ethanol used for the consecutive runs are normalized to the mass of SAPO-35 after recovery.

4. Conclusions

In conclusion, the synthesis and crystallization profiles of SAPO-35 zeolite has successfully been investigated using 1-propylpyridinium hydroxide ([PPy]OH) as a structure-directing agent. By using this novel *N*-heterocyclic organic template, the crystallization time of SAPO-35 is shortened to 21 h as compared to that synthesized using conventional hexamethyleneimine-templating method. In addition, the current work also observes a different crystallization route of SAPO-35 involving dissolution of reactants, nucleation and crystal growth of SAPO-34, followed by intrazeolite transformation from SAPO-34 to SAPO-35. Unlike previous work, the SAPO-35 zeolite synthesized using of [PPy] OH template exhibits high porosity and acidity. The SAPO-35 solid is also active and selective in the catalytic conversion of levulinic acid into ethyl levulinate under non-microwave instant heating where excellent conversion (96.3%) and selectivity (100%) towards ethyl levulinate are achieved (190 °C, 20 min) with high catalyst recyclability. Hence, from the perspective of material science, the current work not only provides an insight into the roles of new pyridinium organic template on the crystallization of SAPO-*n* nanoporous material but also on designing solid catalyst with enhanced properties for green chemistry applications such as catalytic biofuel upgrading and molecular separation processes.

CRediT authorship contribution statement

Yik-Ken Ma: Writing – original draft, Investigation, Formal analysis, Data curation. **Stephen Chia**: Investigation, Formal analysis. **Jean-Louis Paillaud**: Investigation, Formal analysis, Data curation. **T. Jean Daou**: Investigation, Formal analysis, Data curation. **Fitri Khoerunnisa**: Writing – review & editing, Data curation, Conceptualization. **Zeinhom M. El-Bahy**: Investigation, Formal analysis. **Tau Chuan Ling**: Writing – review & editing, Investigation. **Amal A. Altalhi**: Writing – review & editing, Investigation, Funding acquisition, Formal analysis. **Samy F. Mahmoud**: Data curation, Investigation. **Eng-Poh Ng**: Writing – review & editing, Supervision, Project administration, Methodology, Investigation, Funding acquisition, Conceptualization.

Declaration of competing interest

The authors declare that they have no known competing financial interests or personal relationships that could have appeared to influence the work reported in this paper.

Acknowledgements

The financial assistance from RUI (1001/PKIMIA/8011128), Universiti Sains Malaysia, Malaysia is acknowledged. The authors would also like to extend their appreciation to Taif University Researchers Supporting Project (TURSP-2020/243), Taif University, Saudi Arabia for financial support.

Appendix A. Supplementary data

Supplementary data to this article can be found online at https://doi.org/10.1016/j.matchemphys.2022.126240.

References

[1] D.Y. Khoo, W.-M. Kok, R.R. Mukti, S. Mintova, E.-P. Ng, Ionothermal approach for synthesizing AlPO-5 with hexagonal thin-plate morphology influenced by various parameters at ambient pressure, Solid State Sci. 25 (2013) 63–69, https://doi.org/10.1016/j.solidstatesciences.2013.08.008.

[2] Y.X. Liu, H. Yu, X. Liu, N. Zhang, X. Wang, L. Li, S. Yu, Eco-friendly synthesis of hierarchical SAPO-11 with fluoride ions for hydroisomerization of n-hexane, Microporous Mesoporous Mater. 323 (2021), 111229, https://doi.org/10.1016/j.micromeso.2021.111229.

[3] L. Calabrese, L. Bonaccorsi, P. Bruzzaniti, E. Proverbio, A. Freni, SAPO-34 based zeolite coatings for adsorption heat pumps, Energy 187 (2019), 115981, https://doi.org/10.1016/j.energy.2019.115981.

[4] E.-P. Ng, H. Awala, S. Komaty, S. Mintova, Microwave-green synthesis of AlPO-n and SAPO-n (n = 5 and 18) nanosized crystals and their assembly in layers, Microporous Mesoporous Mater. 280 (2019) 256–263, https://doi.org/10.1016/j.micromeso.2019.02.016.

[5] E.-P. Ng, L. Delmotte, S. Mintova, Selective capture of water using microporous adsorbents to increase the lifetime of lubricants, ChemSusChem 2 (2009) 255–260, https://doi.org/10.1002/cssc.200800234.

[6] H. An, H. Li, J. Zhou, J. Zhang, T. Zhang, M. Ye, Z. Liu, Kinetics of steam regeneration of SAPO-34 zeolite catalyst in methanol-to-olefins (MTO) process, Chin. J. Chem. Eng. 35 (2021) 231–238, https://doi.org/10.1016/j.cjche.2021.07.009.

[7] G. Yu, M. Qiu, T. Wang, L. Ge, X. Chen, W. Wei, Optimization of the pore structure and acidity of SAPO-11 for highly efficient hydroisomerization on the long-chain alkane, Microporous Mesoporous Mater. 320 (2021), 111076, https://doi.org/10.1016/j.micromeso.2021.111076.

[8] Y.X. Liu, H. Yu, X. Liu, N. Zhang, X. Wang, L. Li, S. Yu, Eco-friendly synthesis of hierarchical SAPO-11 with fluoride ions for hydroisomerization of n-hexane, Microporous Mesoporous Mater. 323 (2021), 111229, https://doi.org/10.1016/j.micromeso.2021.111229.

[9] T. Blasco, A. Chica, A. Corma, W.J. Murphy, J. Agúndez-Rodríguez, J. P´erez-Pariente, Changing the Si distribution in SAPO-11 by synthesis with surfactants improves the hydroisomerization/dewaxing properties, J. Catal. 242 (2006) 153–161, https://doi.org/10.1016/j.jcat.2006.05.027.

[10] L. Li, K. Shen, X. Huang, Y. Lin, Y. Liu, SAPO-11 with preferential growth along the a-direction as an improved active catalyst in long-alkane isomerization reaction, Microporous Mesoporous Mater. 313 (2021), 110827, https://doi.org/10.1016/j.micromeso.2020.110827.

[11] N. Chen, Y. Ren, E.W. Qian, Elucidation of the active phase in PtSn/SAPO-11for hydrodeoxygenation of methyl palmitate, J. Catal. 334 (2016) 79–88, https://doi.org/10.1016/j.jcat.2015.11.001.

[12] Y.-K. Chen, C.-H. Hsieh, W.-C. Wang, The production of renewable aviation fuel from waste cooking oil. Part II: catalytic hydrocracking/isomerization of hydroprocessed alkanes into jet fuel range products, Renew. Energy 157 (2020) 731–740, https://doi.org/10.1016/j.renene.2020.04.154.

[13] L. Marchese, A. Frache, G. Gatti, S. Coluccia, L. Lisi, G. Ruoppolo, G. Russo, H. O. Pastore, Acid SAPO-34 catalysis for oxidative dehydrogenation of ethane, J. Catal. 208 (2002) 479–484, https://doi.org/10.1006/jcat.2002.3578.

[14] J. Yu, R. Xu, Insight into the construction of open-framework aluminophosphates, Chem. Soc. Rev. 35 (2006) 593–604, https://doi.org/10.1039/B505856M.

[15] I. Pinilla-Herrero, U. Olsbye, C. Márquez-Álvarez, E. Sastre, Effect of framework topology of SAPO catalysts on selectivity and deactivation profile in the methanolto-olefins reaction, J. Catal. 352 (2017) 191–207, https://doi.org/10.1016/j.jcat.2017.05.008.

[16] B.M. Lok, C.A. Messina, R.L. Patton, R.T. Gajek, T.R. Cannan, E.M. Flanigen, Crystalline Silicoaluminophosphates, United States Patents US4440871A, 1982.

[17] U. Lohse, F. Vogt, J. Richter-Mendau, Synthesis and characterization of the levynelike structure SAPO-35 prepared with cyclohexylamine as templating agent, Cryst. Res. Technol. 28 (1993) 1101–1107, https://doi.org/10.1002/crat.2170280812.

[18] P.A. Barrett, R.H. Jones, J.M. Thomas, G. Sankar, I.J. Shannon, C.R.A. Catlow, Rational design of a solid acid catalyst for the conversion of methanol to light alkenes: synthesis, structure and performance of DAF-4, Chem. Commun. 382 (1996) 2001–2002, https://doi.org/10.1039/CC9960002001.

[19] N. Venkatathri, J.W. Yoo, Synthesis, characterization and catalytic properties of a LEV type silicoaluminophosphate molecular sieve, SAPO-35 from aqueous media using aluminum isopropoxide and hexamethyleneimine template, Appl. Catal. AGen. 340 (2008) 265–270, https://doi.org/10.1016/j.apcata.2008.02.026.

[20] S. Siliveri, S.S.K. Pinnepalli, D. Joshi, S. Chirra, S. Goskula, S.R. Gujjula, N. A. Oyler, V. Narayanan, Investigation on the promoter-induced rapid non-aqueous media synthesis of SAPO-35 and methanol-to-olefin reaction, ACS Omega 6 (2021) 5661–5669, https://doi.org/10.1021/acsomega.0c06109.

[21] Y. Huang, H. Ma, Z. Xu, W. Qian, H. Zhang, W. Ying, Utilization of SAPO-18 or SAPO-35 in the bifunctional catalyst for the direct conversion of syngas to light olefins, RSC Adv.. 11 (23) 13876-13884. https://doi.org/10.1039/D1RA02087K.

[22] J. Heda, P. Niphadkar, S. Mudliar, V. Bokade, Highly efficient micro-meso acidic HUSY catalyst for one step conversion of wheat straw to ethyl levulinate (biofuel additive), Microporous Mesoporous Mater. 306 (2020), 110474, https://doi.org/10.1016/j.micromeso.2020.110474.

[23] D. Obermayer, D. Znidar, G. Glotz, A. Stadler, D. Dallinger, C.O. Kappe, Design and performance validation of a conductively heated sealed-vessel reactor for organic synthesis, J. Org. Chem. 81 (2016) 11788–11801, https://doi.org/10.1021/acs.joc.6b02242.

[24] J.B.d. Heredia, J.R. Domínguez, Y. Cano, I. Jim´enez, Nitrate removal from groundwater using Amberlite IRN-78: modelling the system, Appl. Surf. Sci. 252 (2006) 6031–6035, https://doi.org/10.1016/j.apsusc.2005.11.030.

[25] M. Halder, P. Bhanja, M.M. Islam, S. Chatterjee, A. Khan, A. Bhaumik, S.M. Islam, Porous organic polymer as an efficient organocatalyst for the synthesis of biofuel ethyl levulinate, Mol. Catal. 494 (2020) 111119, https://doi.org/10.1016/j.mcat.2020.111119.

[26] U. Mandi, N. Salam, S.K. Kundu, A. Bhaumik, S.M. Islam, Ruthenium nanoparticles supported over mesoporous TiO2 as an efficient bifunctional nanocatalyst for esterification of biomass-derived levulinic acid and transfer-hydrogenation reactions, RSC Adv. 6 (2016) 73440–73449, https://doi.org/10.1039/C6RA10233F.

[27] E.-P. Ng, L. Itani, S.S. Sekhon, S. Mintova, Micro- to macroscopic observations of MnAlPO-5 nanocrystal growth in ionic-liquid media, Chem. Eur J. 16 (2010) 12890–12897, https://doi.org/10.1002/chem.201001083.

[28] S.-F. Wong, H. Awala, A. Vincete, R. Retoux, T.C. Ling, S. Mintova, R.R. Mukti, E.-P. Ng, K-F zeolite nanocrystals synthesized from organic-template-free precursor mixture, Microporous Mesoporous Mater. 249 (2017) 105–110, https://doi.org/10.1016/j.micromeso.2017.04.053.

[29] S. Sogukkanli, K. Iyoki, S.P. Elangovan, K. Itabashi, T. Okubo, Seed-directed synthesis of CON-type zeolite using tetraethylammonium hydroxide as a simple organic structural directing agent, Chem. Lett. 46 (2017) 1419–1421, https://doi.org/10.1246/cl.170602.

[30] K. Muraoka, Y. Sada, A. Shimojima, W. Chaikittisilp, T. Okubo, Tracking the rearrangement of atomic configurations during the conversion of FAU zeolite to CHA zeolite, Chem. Sci. 10 (2019) 8533–8540, https://doi.org/10.1039/C9SC02773D.

[31] IZA-SC, Database of Zeolite Structures, 2021. http://www.iza-structure.org/databases/. (Accessed 12 November 2021).

[32] J.N. Appaturi, R.J Ramalingam, H.A. Al-Lohedan, F. Khoerunnisa, T.C. Ling, E.-P. Ng, Selective synthesis of dioxolane biofuel additive via acetalization of glycerol and furfural enhanced by MCM-41-alanine bifunctional catalyst, Fuel 288 (2021) 119573,

https://doi.org/10.1016/j.fuel.2020.119573.

[33] S.-F. Wong, K. Deekomwong, J. Wittayakun, T.C. Ling, O. Muraza, F. Adam, E.-P. Ng, Crystal growth study of K-F nanozeolite and its catalytic behavior in Aldol condensation of benzaldehyde and heptanal enhanced by microwave heating, Mater. Chem. Phys. 196 (2017) 295–301. https://www.sciencedirect.com/science/article/pii/S0254058417303437.

[34] J. Li, Z. Li, D. Han, J. Wu, Facile synthesis of SAPO-34 with small crystal size for conversion of methanol to olefins, Powder Technol. 262 (2014) 177–182, https://doi.org/10.1016/j.powtec.2014.04.082.

[35] H. van Heyden, S. Mintova, T. Bein, Nanosized SAPO-34 synthesized from colloidal solutions, Chem. Mater. 20 (2008) 2956–2963, https://doi.org/10.1021/cm703541w.

[36] P. Niu, X. Ren, D. Xiong, S. Ding, Y. Li, Z. Wei, X. Chen, Synthesis of highly selective and stable Co-Cr/SAPO-34 catalyst for the catalytic dehydration of ethanol to ethylene, Catalysts 10 (2020) 785, https://doi.org/10.3390/catal10070785.

[37] G. Liu, P. Tian, J. Li, D. Zhang, F. Zhou, Z. Liu, Synthesis, characterization and catalytic properties of SAPO-34 synthesized using diethylamine as a template, Microporous Mesoporous Mater. 111 (2008) 143–149, https://doi.org/10.1016/j.micromeso.2007.07.023.

[38] S. Askari, R. Halladj, M. Sohrabi, Methanol conversion to light olefins over sonochemically prepared SAPO-34 nanocatalyst, Microporous Mesoporous Mater. 163 (2012) 334–342, https://doi.org/10.1016/j.micromeso.2012.07.041.

[39] S. Cheng, J.-N. Tzeng, B.-Y. Hsu, Synthesis and characterization of a novel layered aluminophosphate of Kanemite-like structure, Chem. Mater. 9 (1997) 1788–1796, https://doi.org/10.1021/cm9700357.

[40] D.Y.Y. Khoo, H. Awala, S. Mintova, E.-P. Ng, Synthesis of AlPO-5 with diolsubstituted imidazolium-based organic template, Microporous Mesoporous Mater. 194 (2014) 200–207, https://doi.org/10.1016/j.micromeso.2014.04.010.

[41] K.S.W. Sing, D.H. Everett, R.A.W. Haul, L. Moscou, R.A. Pierotti, J. Rouquerol, T. Siemieniewska, Reporting physisorption data for gas/solid systems with special reference to the determination of surface area and porosity, Pure Appl. Chem. 57 (1985) 603–619, https://doi.org/10.1351/pac198254112201.

[42] F. Adam, J.N. Appaturi, E.-P. Ng, Halide aided synergistic ring opening mechanism of epoxides and their cycloaddition to CO2 using MCM-41-imidazolium bromide catalyst, J. Mol. Catal. Chem. 386 (2014) 42–48, https://doi.org/10.1016/j.molcata.2014.02.008.

[43] Y. Lyu, Y. Liu, X. He, L. Xu, X. Liu, Z. Yan, The regulation of Si distribution and surface acidity of SAPO-11 molecular sieve, Appl. Surf. Sci. 453 (2018) 350–357, https://doi.org/10.1016/j.apsusc.2018.05.106.

[44] M.-Y. Choo, L.E. Oi, T.C. Ling, E.-P. Ng, Y.-C. Lin, G. Centi, J.C. Juan, Deoxygenation of triolein to green diesel in the H2-free condition: effect of transition metal oxide supported on zeolite Y, J. Anal. Appl. Pyrolysis 147 (2020), 104797, https://doi.org/10.1016/j.jaap.2020.104797.

[45] E.-P. Ng, J.-H. Chow, R.R. Mukti, O. Muraza, T.C. Ling, K.-L. Wong, Hydrothermal synthesis of zeolite a from bamboo leaf biomass and its catalytic activity in cyanoethylation of methanol under autogenic pressure and air conditions, Mater. Chem. Phys. 201 (2017) 78–85, https://doi.org/10.1016/j.matchemphys.2017.08.044.

[46] N.H. Ahmad, T.J. Daou, P. Maireles-Torres, M. Zaarour, S. Mintova, T.-C. Ling, E.-P. Ng, Morphological effects on catalytic performance of LTL zeolites in acylation of 2-methylfuran enhanced by non-microwave instant heating, Mater. Chem. Phys. 244 (2020), 122688, https://doi.org/10.1016/j.matchemphys.2020.122688.

[47] M.J. Ginés-Molina, N.H. Ahmad, S. Mérida-Morales, C. Garcia-Sancho, S. Mintova, E.-P. Ng, P. Maireles-Torres, Selective conversion of glucose to 5-Hydroxymethylfurfural by using L-Type zeolites with different morphologies, Catalysts 9 (2019) 1073, https://doi.org/10.3390/catal9121073.

[48] V.M. Georgieva, E.L. Bruce, M.C. Verbraeken, A.R. Scott, W.J. Casteel Jr., S. Brandani, P.A. Wright, Triggered gate opening and breathing effects during selective CO2 adsorption by merlinoite zeolite, J. Am. Chem. Soc. 141 (2019) 12744–12759, https://doi.org/10.1021/jacs.9b05539.

[49] V. Babic, Increasing the porosity of zeolites, Catalysis (2021). https://tel.archives-ouvertes.fr/tel-03167919.

[50] K.Y. Nandiwale, V.V. Bokade, Environmentally benign catalytic process for esterification of renewable levulinic acid to various alkyl levulinates biodiesel, Environ. Prog. Sustain. Energy 34 (2014) 795–801, https://doi.org/10.1002/ep.12042.

[51] J.G. Smith, Organic Chemistry, fifth ed., McGraw Hill, New York, 2017.

[52] M. Shokouhimehr, Magnetically separable and sustainable nanostructured catalysts for heterogeneous reduction of nitroaromatics, Catalysts 5 (2015) 534–560, https://doi.org/10.3390/catal5020534.